PNAS
www.pnas.org

Supporting Information for

Valveless microliter combustion for densely packed arrays of powerful soft actuators

Ronald H. Heisser, Cameron A. Aubin, Ofek Peretz, Nicholas Kincaid, Hyeon Seok An, Elizabeth M. Fisher, Sadaf Sobhani, Perrine Pepiot, Amir Gat, and Robert F. Shepherd

Robert F. Shepherd
Email: rfs247@cornell.edu

This PDF file includes:

Other supplementary materials for this manuscript include the following:

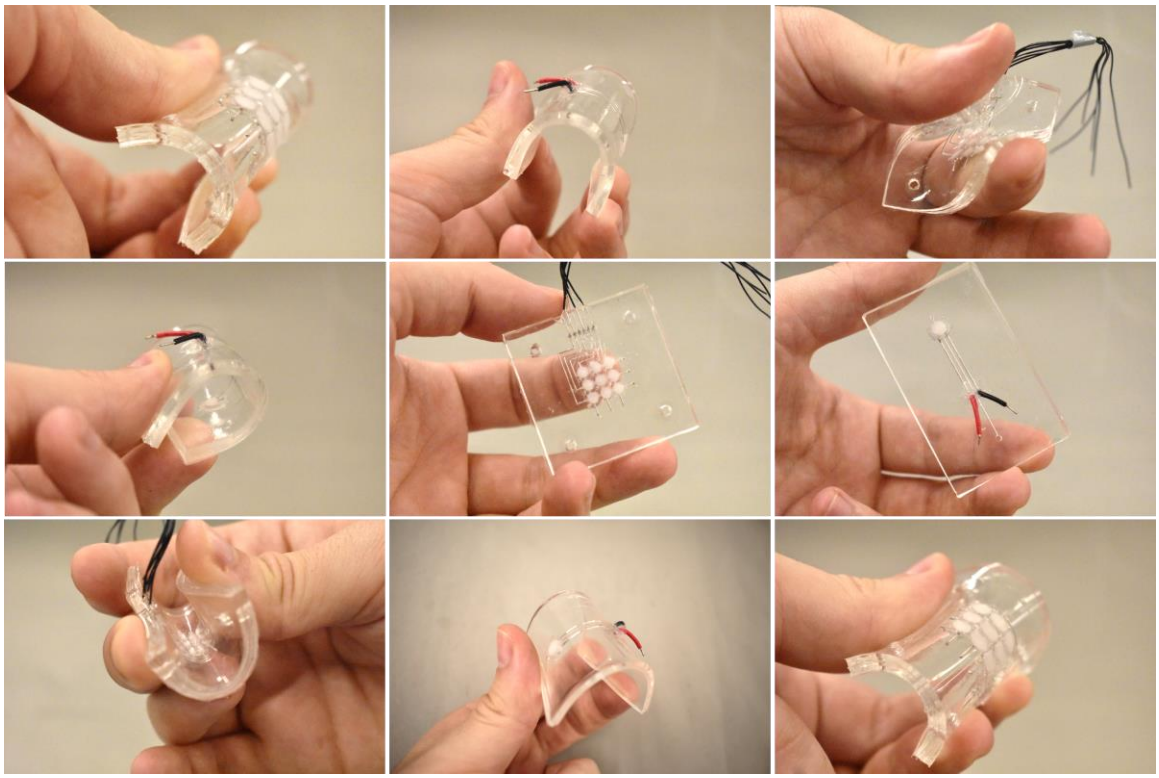

Fig. S1. Soft Actuator Compliance. The single cylinder and arrayed actuators can be deformed into many high curvature configurations without losing their constitution.

0. Experimental Combustion Safety

Gaseous combustible mixtures are highly reactive and should be treated as potentially dangerous at any volume. Experimental environments should be designed and operated to protect researchers from worst-case failures. These experiments took place in a lab space not initially designed to study combustion. The use of flammable gases is often covered by building and fire codes, providing one basis to establish these types of experiments. We corresponded with Cornell Environmental Health and Safety (EH&S) officers to ensure compliance with campus regulations and local codes. In general, researchers should be prepared to share a piping and instrumentation diagram (P&ID) with safety personnel who have prior experience in failure modes to safely design and implement their own experimental environment.

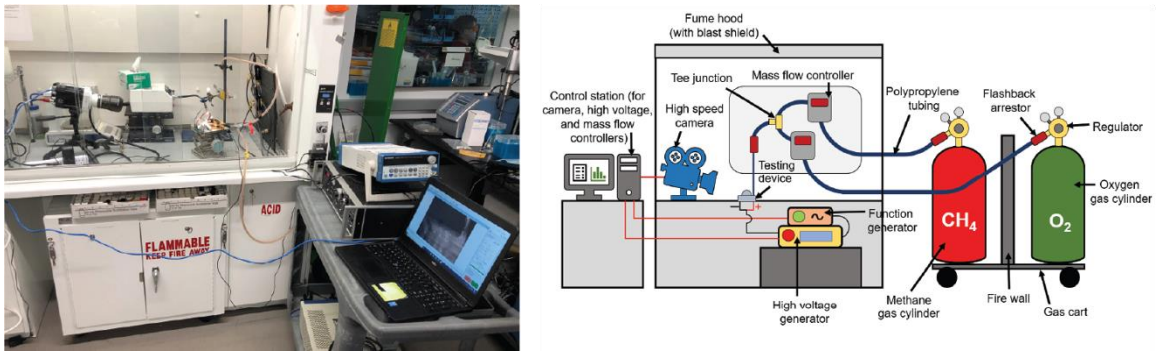

Fig. S2. Experimental Environment and P&ID.

We tested devices in a constant flow fume hood and did not exceed 5 mL s^{-1} flow of methane. Calculations were done to keep methane accumulation below the Lower Explosive Limit

(LEL) in the building ductwork, to avoid downstream duct explosions. Digital mass flow controllers (MFCs) precisely managed concentrations of methane and oxygen and were unplugged after each experiment. Flame arrestors placed downstream of gas control components prevented unwanted flame backpropagation. At least two people were present for all experiments. A small blast shield was also used as a precautionary measure. Flame proof lab coats, goggles, and ear protection served as adequate PPE for small-scale combustion testing.

1. Design and Manufacturing

1.1 Single Cylinder Actuator. We designed the single cylinder actuator to be a concept validation platform. The planar arrangement of chamber, gas channels, and electrode channels reduced the design to one functional layer and simplified design iterations. We focused our tests on one actuator geometry, which comprised a combustion chamber of 5 mm diameter and 2 mm depth, an intake channel with 0.4 x 0.4 mm^2 area, a surface exhaust port with 0.75 mm diameter, and electrode channels with 0.4 x 0.3 mm^2 area. Channel and port dimensions were chosen to comfortably match additive manufacturing resolution (30 μm for a polyjet printer, Stratasys Objet30 Scholar and VeroBlue™ photopolymer). The following steps describe the single cylinder actuator manufacturing process:

1. We prepared the PDMS prepolymer resin by first mixing components in a Thinky planetary centrifugal mixer at 2,000 rpm for one minute.
2. Next, we poured the liquid PDMS prepolymer into actuator and base layer molds and degassed them for 20 minutes.
3. We finished fabricating the actuator layers by curing the PDMS in a constant temperature oven (80 °C) for at least 1 hour.
4. To adhere the actuator layer to the base layer, we first doctor-bladed a thin film (10-30 μm) of the same PDMS liquid prepolymer onto a glass plate.
5. Then we lightly placed the actuator layer on the liquid layer and quickly peeled it off to prevent the liquid PDMS from infiltrating and blocking the gas channels.
6. We completed the initial structure of the device by placing the actuator layer on base layer and lightly tapping bubbles out from the sides with tweezers to ensure complete lamination. Then we cured the PDMS in the oven again for at least 1 hour.
7. Next, we injected liquid metal (LM) into electrode channels to form the spark gap igniter.
8. Then, we inserted solid-core breadboard wire leads into back ends of electrode channels and poured additional polymer at the press-fit interface. We cured the device again in the oven for not less than 1 hour.
9. We formed the membrane simply by punching out a 0.5 mm thick, 7 mm diameter Ecoflex disc from a premade sheet, with a leather hole punch.
10. We then attached the membrane to top of the actuator cylinder with silicone epoxy and cured the device in the oven again, for at least 30 minutes.
11. To make the device operational, we press-fit an external fuel delivery tube into the back of the intake channel and connect the open wire leads to a high voltage (HV) control output.

1.2 Arrayed Actuator. The arrayed actuator follows the same manufacturing principles as the single cylinder actuator: We mold four, separate, 1 mm-thick layers of the array and bond them together with liquid PDMS prepolymer using steel dowel pins. The constant temperature oven completed curing between bonding steps. Below, we list the additional steps we took to scale our concept further.

1. First, we formed the electrical insulation layer by “drip coating” PDMS prepolymer on an acrylic plate, then hanging it on its side for at least one day to allow for excess liquid to

drain off the edge and room temperature curing, resulting in final layer thicknesses between 20 µm and 50 µm.

2. Then, once the fuel layer was bonded to the two sets of electric traces, we placed a sintered metal disc inside the fuel layer, directly under the device supply gas tube.
3. Before bonding the cylinder layer to the fuel layer, we fed 34AWG wires into the six small openings to connect to the LM traces.
4. After the cylinder layer was bonded, we formed electrodes in each combustion cylinder to make the spark gaps.
    - For each spark gap, we manually pierced one end of a stripped 34AWG wire segment completely through the fuel layer, and through the entire electrode channel. The other wire end was pierced into the wall of the inlet opening.
    - Then, we bent the wires and moved them towards each other to form a small spark gap (< 1 mm). Fig. S3 illustrates rendered and functional visualization of the spark gap formed in an individual cylinder.

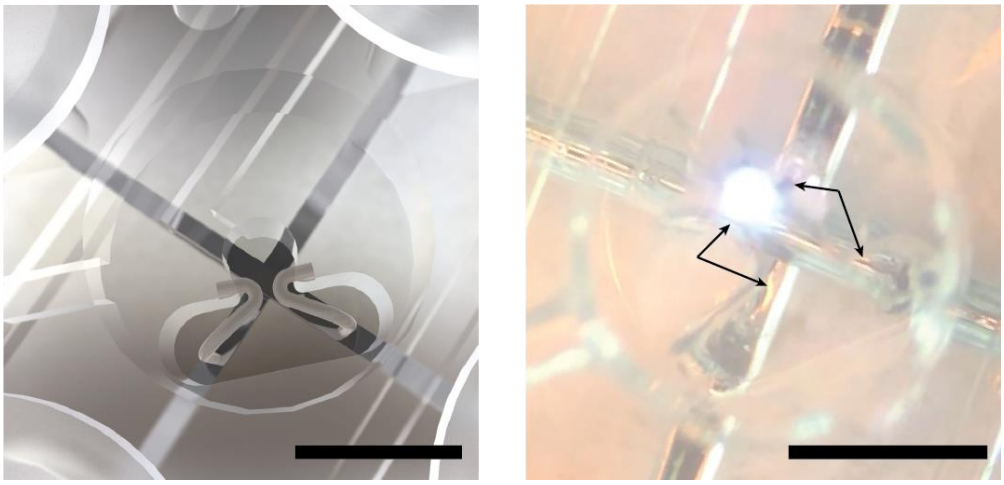

Fig. S3. Array Spark Gap Wiring Detail. Each picture shows a unit cylinder without the membrane top to reveal the internal architecture. Left panel is a rendering of an assembled actuator. Right panel is a picture taken from the eyepiece of a binocular stereo microscope (overhead illumination). Light in center is electric arc. Arrows point towards piercing ends of wires. Scale bars: 1.5 mm.

1.3 Spark Demultiplex Control Electronics. To prove that electric breakdown, a phenomena usually associated with loss of control or failure, can be exploited to control our array, we designed a rudimentary electronic circuit which transfers input from a single HV amplifier to the appropriate LM traces. Reducing electric component count is important for these applications, as piezoelectric refreshable braille displays often include one HV (~300 V) driver circuit for each braille cell, which also contributes to high device costs (1). Therefore, we connected each electrical trace to one HV relay and further upstream to the single amplifier. We used HV reed relays (KT05-1A-40L-SMD, Standex Electronics, Inc., and 5503-05-1, Coto Technology, Inc.) organized on two small copper PCB prototyping plates. Fig. S4 shows two assemblies with which we tested individual spark control. Through the relays, widthwise LM traces connected to the common +V terminal of the HV amplifier. The lengthwise traces connected to the common ground (GND) terminal. We controlled relay switching with Arduino UNO digital output ports.

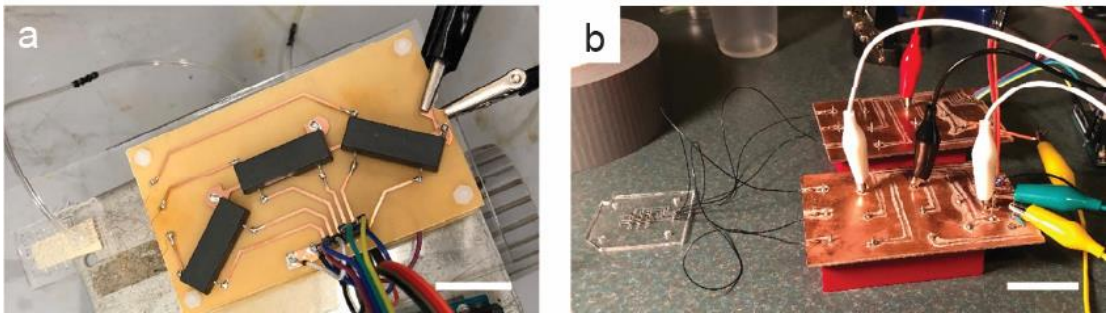

Fig. S4. HV Reed Relay Circuit Prototypes. (a) FR1 PCB copper trace negatives were cut away with a desktop CNC milling machine (monoFab SRM-20, Roland DGA Corp.) to connect two sets of three HV reed relays (Standex) to the device and common inputs. These relays are rated for 1 kV switching. Relays were stacked on top of each other and separated with nylon standoffs at the corners. Scale bar: 50 mm. (b) A separate design was hand routed with a Dremel tool and connected to 3 kV rated HV relays (Coto), one being visible as the red rectangle under the nearest PCB. This design included the miniature HV amplifier (EMCO Q20-5, XP Power). Scale bar: 100 mm.

Because the relays operate via large inductors, switching the relay on produced a counter-electromotive spike in the coil >100 V. Occasionally, these spikes would interfere with the microcontroller clock cycles and cause the switching procedure to repeat individual steps or itself entirely. We suspect that the interrupted switching also causes switch bouncing (2). We mitigated these problems by setting a delay time of 100 ms between each relay switch. This helped decrease the frequency of failure; future iterations will incorporate appropriate debouncing components (such as a low pass filter) to enable cleaner electronic operation. Sub-mm, demultiplexed spark ignition is not commonly implemented in electronic systems. Since sparks need only persist for an instant (~1 µs) to trigger combustion, we expect that these operating cycles can be reduced to the µs scale without any significant innovations.

1.4 Design for Scale. Currently, piezoelectric refreshable braille displays are the only commercially available technology (this excludes vibrotactile systems and some single line displays), usually at a cost of thousands to tens of thousands of dollars for a single device. We believe that our arrayed actuator has potential to power a full-page braille display. Given the braille cell design specifications, 2 mm diameter combustion chambers can comfortably lie below and actuate braille dots. We can then roughly estimate the material cost for our actuator. Consider a cylindrical actuator unit including close interstitial material around it, having dimensions of 2.5 x 2.5 x 4 mm^3. Neglect the cost of the spark gap wire piercings. Assume that a single sheet of Ecoflex covers the entire surface area. If all other material dimensions are kept constant, then a single actuator would have 17.9 µL of PDMS, 40 nL of liquid gallium, and 1.9 µL of Ecoflex. Given respective per-kg material costs of $200, $350, and $45 (taken from Amazon product searches), the functional components of a single actuator would have 0.39¢ material costs. If sintered filters are ultimately required for each actuator, this would likely increase the unit cost above 1¢. Currently, HV relays, DC-HVDC components, and a microcontroller would add ~$500 to the total cost, yet would be ‘amortized’ as the number of actuators increases.

Currently, the fuel manifold layer is the only component that we did not make simply scalable. All fuel channels branched directly from the inlet gas source to eliminate crosstalk and share one sintered disc filter. Future channel and port dimensions can be significantly reduced at the expense of maximum flow rates.

One of the important technological challenges for tactile display development is to make devices portable and capable of long-term untethered operation. Our proposed technology requires both batteries and onboard fuel storage to be portable. However, fuels such as butane can be reliably stored at room temperature in liquid phase. An 18 cc container of liquid butane is equal in mass to 4,000 cc of gaseous butane. For comparison, a 2 mm diameter, 1 mm height cylinder has a volume of 0.003 cc. A full-page braille display (25 lines, 40 cells per line) has 6,000 dots. Neglecting

oxidizer gas, the 18 cc liquid butane container alone has enough gas to fill the entire page ~222 times before becoming empty. Stoichiometric oxy-butane gas is 13.3% butane; the amount required for our purposes may be significantly less than stoichiometric, thus the real use time per canister stands to be even higher.

2. Experimental Details

2.1 Experimental Apparatus. We conducted experiments in a fume hood equipped with appropriate blast and flame protection (See Fig. S2). A single computer controlled the oxygen and methane MFCs (M-100SCCM-D, Alicat Scientific) and the high-speed camera. We varied the camera frame rate to balance image luminance. With a separate computer, we powered and adjusted the Arduino protocols. Gas was injected into the device via soft plastic (Tygon) tubes downstream of a Y-connector to ensure the fuel was mixed. The mixing length was ~1 m. Prototype devices were placed on a manually adjustable Z stage. A fiber optic illuminator focused high-intensity light on the membrane for high-speed videography. A function generator (4084AWG, BK Precision) connected to an HV amplifier (Model 50/12, Trek, Inc.) precisely controlled sparking for frequency response tests. Initially, we used a compact DC-HVDC amplifier (EMCO Q20-5, XP Power) directly mounted on the HV relay switchboard to generate sparks in the array, later breaking from mishandling. In general, these small HV amplifiers function well in this application, and can consume less than 0.5 W, increasing the operational efficiency of our system (see SI Appendix, 3.2). We then used the TREK amplifier with the function generator set at DC for remaining tests. When operational, the EMCO module produced satisfactory results.

The main text discusses characterization of a 5 mm diameter, 2 mm thick single cylinder actuator and demonstration of a 3 mm diameter, 1 mm thick arrayed actuator. Several smaller geometries were tested, though not reported in the main text. Generally, as an enclosing volume decreases, combustion is more strongly inhibited by walls through flame-wall heat conduction and wall radical quenching (3). We find that our actuators successfully undergo oxy-fuel combustion at low stoichiometries. High Φ operation should enable smaller-footprint actuations. Indeed, we have colloquially observed the actuation of a 1 mm diameter, 2 mm thick single cylinder actuator for a mixture of $\Phi \approx 0.75$, shown in Fig. S5.

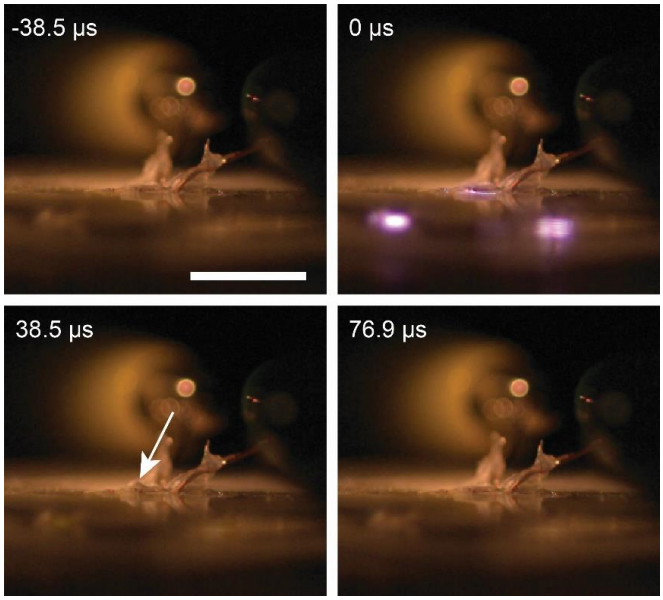

Fig. S5. 1mm Diameter Single Cylinder Actuation. Four consecutive frames shot at 26,000 fps (Phantom) show initial results for 1 mm-diameter, 0.3 mm thick membrane displacement. Third frame (white arrow) shows approximate displacement in the range of 0.5-1 mm. 0 µs frame shows blue light from the ignition plasma. Out-of-focus objects in background are alligator clips attached to wire leads sealed with silicone epoxy (Sil-Poxy, Smooth On, Inc). Operated at $\Phi \approx 0.75$. Scale bar: 10 mm.

2.2 Inflation Measurements. Membranes were assumed to undergo axisymmetric deformations; we informed our analysis using videos taken at the side of the actuator. When the cylinder is full of reactant gas, actuations are visible to the naked eye as flickers of motion. Review of high-speed videos shows much richer dynamics within the actuation timescale: the membrane's general inflation and deflation cycle occurs in concert with smaller, higher-order oscillations (4). Given the extremely low membrane inertia and the constant external atmospheric pressure, these oscillations likely reflect gaseous thermal fluctuations and effects of nonlinear membrane elasticity.

2.3 Force Measurements from a Cantilevered Load Cell. We conducted an additional set of experiments intended to give a more direct measure of actuator force and energy output. While motors and engines are generally classified by relating the torque τ to the continuous rotational velocity ω, this actuator does work through impulses. Therefore, we used a cantilevered load cell (S100 0.4 N, Strain Measurement Devices) with a high displacement range to examine what elastic energy could be stored in the load cell by the membrane (cantilever spring constant k ~120 N m^{-1}). For each Φ tested, we varied the initial separation distance between the actuator membrane and sensor to obtain the force and energy output for different amounts of possible engagement between the membrane and the sensor. In this way, we attempted to report results between "full contact force" and "no contact displacement", two extremes analogous to the stall torque and no-load speed that motor specifications commonly give. Then, the membrane does work on the cantilever after contacting it.

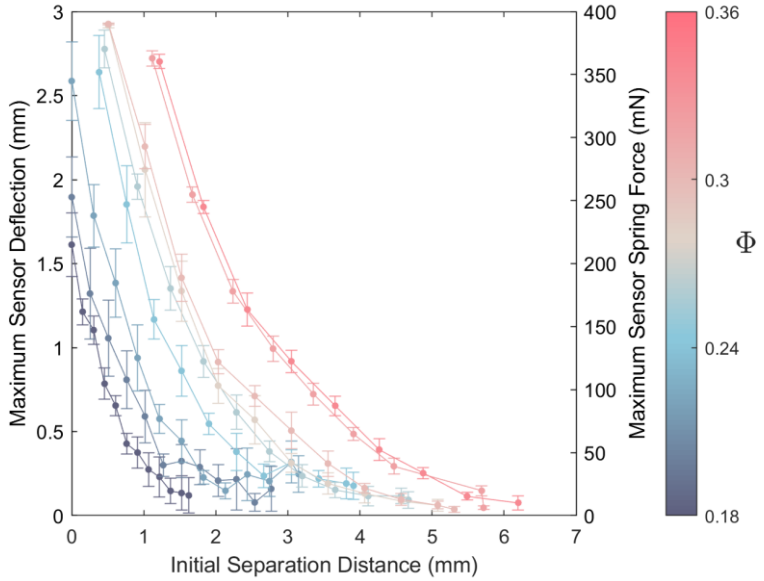

Fig. S6. Cantilevered Load Cell Force Measurements.

To take data, a computer recorded prescribed segments of continuous serial data from an Arduino Wheatstone amplifier shield (RobotShop) with a MATLAB script. Recording sequences were manually triggered in conjunction with manual grill spark ignition of the actuator. We eliminated any silicone membrane stickiness by rubbing a thin layer of talcum powder (Gold Bond™, Sanofi) onto the top of the membrane. This also explains the opaque, white appearance of the membrane in Fig. 1 of the main text. After each experiment, the cylinder was replenished with new reactant gas for 15-20 seconds. Results are shown in Fig. S6, where each data point is an average of at least 10 measurements. Error is calculated from the deflection measurement variance because force output was determined by multiplying the measured displacements by k. Fig. S6 shows a maximum reported force output of 380 mN, which corresponds to a spring elastic energy

output of 1.1 mJ. This is of the same energy scale as the free-inflation device work output reported in the Main Text (W_s = 1.7 mJ). Losses from mechanical coupling are expected, and we believe that the lower work output will remain useful for various applications.

Several measurements were excluded after finding that the sensor output saturates at ~3 mm displacements. Given that the incomplete curves follow the same trends as complete curves, one can reasonably assume that at the maximum stoichiometry used in these experiments (Φ = 0.34), the actuator can impart ~600 mN of force onto this sensor. While this experiment provides some useful insights, a more revealing experiment would determine output force and energy as a function of k to possibly find a critical k at which the highest energy output occurs.

Because this actuator acts within a fast timescale and exerts sub-Newton forces, the coupled mechanical response of the measurement system impacts measurement values. Simple spring-mass modeling suggests that neglecting the inertial resistance results in an underestimation of the applied forces. In other words, some of the combustive energy becomes kinetic energy in the sensor, instead of spring energy. Future experimental design and analysis will produce theoretical corrections to these types of measurements.

2.4 Single Cylinder Exhaust Schlieren Imaging. In the absence of high-fidelity pressure and temperature data, we instead qualitatively studied exhaust using Schlieren imaging techniques. We aligned a parabolic mirror with a point light source, diffracted by the edge of a standard razor blade, to produce the image. The translucent membrane and PDMS substrate side wall did not allow for internal flow visualization. However, we could clearly see exhaust flow during combustion, given the increased gas temperature.

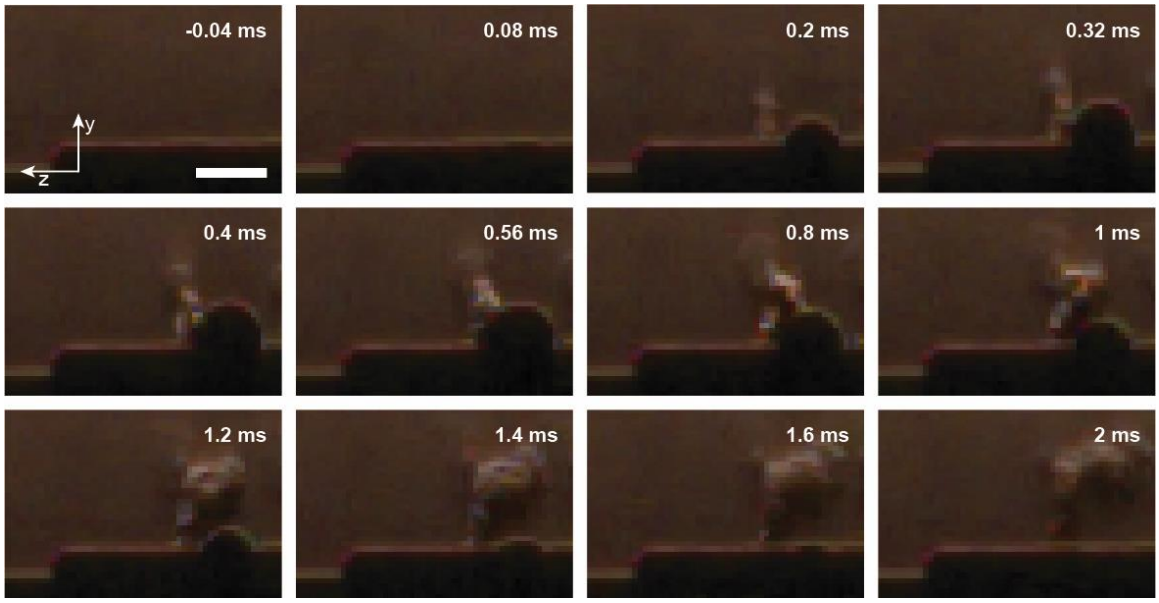

Fig. S7. Selected Schlieren Exhaust Frames. 0 ms corresponds to the moment ignition occurs. The exhaust trail is to the left of the membrane, which appears as an opaque bubble. The full Schlieren video had duplicate imaging due to camera-mirror misalignment; frames are cropped to prevent confusion. Video taken at 25,000 fps. Experiment conducted at Φ = 0.30. Scale bar: 5 mm.

From Fig. S7, we can clearly see hot exhaust flow after actuation begins. Such losses may be undesirable, but we think that most of the gas remains within the enclosed volume during inflation. Future valveless designs can optimize the balance between exhaustion, cylinder refilling time, and the maximum desired stroke distance. Miniature check valves will allow passive exhaustion as the cylinder idles, then prevent exhaustion during combustion and actuation (5).

2.6 Thermoelastic Wear Evaluation. During high-frequency (>1 Hz) operation, the thin silicone membrane encounters repeated exposure to hot flames coupled with high strain deflections. Therefore, the actuator's tolerance of these temperatures partially determines its utility as a viable technology. We performed preliminary life cycle studies of the single cylinder actuator to initially characterize this property of the system, giving intuition for how such a device should be expected to perform over longer timescales.

Room temperature vulcanization (RTV) silicones are known to be stable and maintain their hyperelastic properties at over 150 °C. Other high temperature vulcanization (HTV) rubbers have even higher thermal tolerances. In our case, the silicone membrane must withstand both the bulk heated combustion products and the brief exposure to flames which can exceed 1000 °C.

Fig. S8 shows the results of wear and steady-state thermal tests. All tests were done with a 1.2 mL s^{-1} flow rate. We conducted the wear test at $\Phi = 0.28$ and a 10 Hz sparking frequency. The actuator ran constantly for 2 hours, corresponding to approximately 36,000 consecutive actuations. Data was taken by periodically recording actuation samples with a high speed camera. Fig. S8a shows that the displacement amplitude increases somewhat over time. We suspect that this is due to thermal softening, and not plastic deformation. Additional analysis is needed to confirm this. Visual inspection showed virtually no change in the state of the actuator. We do not consider the flame exposure effects beyond noticing minute amounts of silicate formation towards the center of the membrane. For the applications we describe in the main text, this test represents an extreme use case.

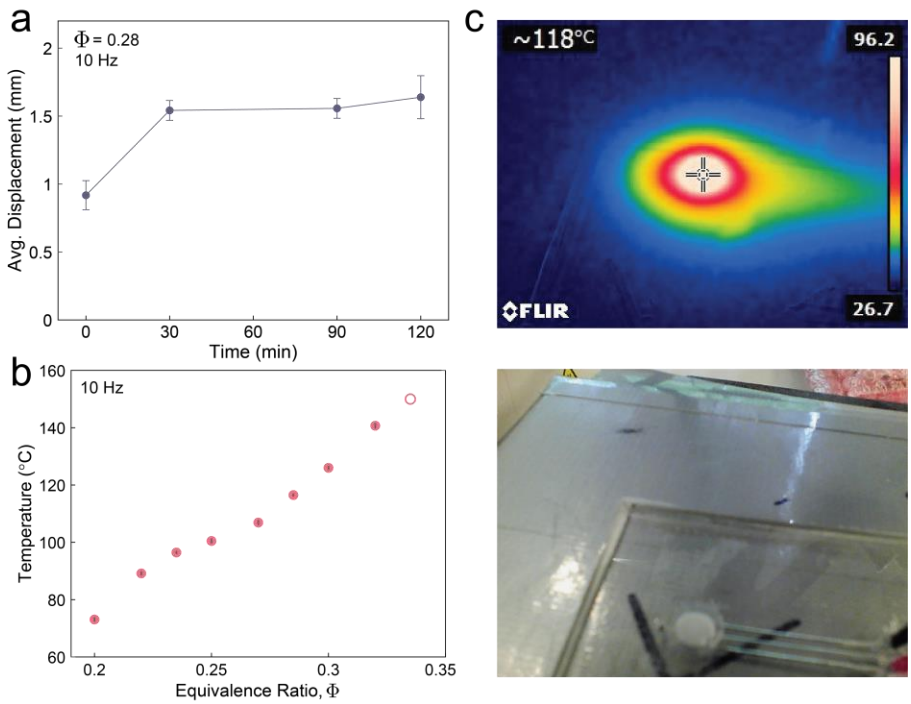

Fig. S8. Thermal and Wear Test Results. (a) Wear test shows average displacements from sample videos taken over the course of 2 hours. No data collected for 1 hour mark. (b) Average temperature recorded after device reached a steady state. Last data point is not filled to note that the membrane broke soon after test began at that stoichiometry. Small dashes inset in the data points show the standard deviation. (c) Infrared image shows temperature distribution on surface of actuator. Temperature measurements were taken from the center of the membrane as the center had the highest temperature. Heat transfer appears biased towards the upstream portion of the inlet fuel channel. An accompanying image from the non-infrared camera is included.

For intermittent actuations, the thermal pulse from combustion produces a negligible change in membrane and actuator temperature. The stability of high frequency actuation depends

in part on actuator thermal loading. Therefore, we measured the steady state temperature achieved by cyclic actuation (also at 10 Hz) for the range of stoichiometries reported in the main text. Fig. S8b shows an approximately linear relationship between steady state temperature and Φ. The actuator was sparked and monitored by an infrared camera (E4, Teledyne FLIR) until the temperature fluctuated within 2 °C of a maximum temperature, shown in Fig. S8c. The actuator eventually failed in the center at the highest stoichiometry we tested, noted by the open ring in Fig S7b.

Continuous gas flow contributes to convection which likely helps to maintain a lower temperature. Higher flow rates would increase convection but also increase the amount of reactant available for each combustion. The relationship between the cooling and heating properties of the flowing gas should be explored further. Other hyperelastic rubbers should be investigated for their thermal tolerance properties, as this study only investigated the performance of one material (Ecoflex 00-30).

2.7 Actuator Array Demonstration. We fabricated an array of 9 actuators in a square, 3x3 arrangement. Counting only the square surrounding these actuators, this array has an actuator density of 0.075 mm^{-2}, and each actuator has a footprint of ~7 mm^2. These dimensions were chosen to maintain manufacturing simplicity. Individual actuator control was proven through manually igniting each of the nine cylinders and taking high speed video of their subsequent displacements. Fig. S9 shows stills of individual actuator displacements.

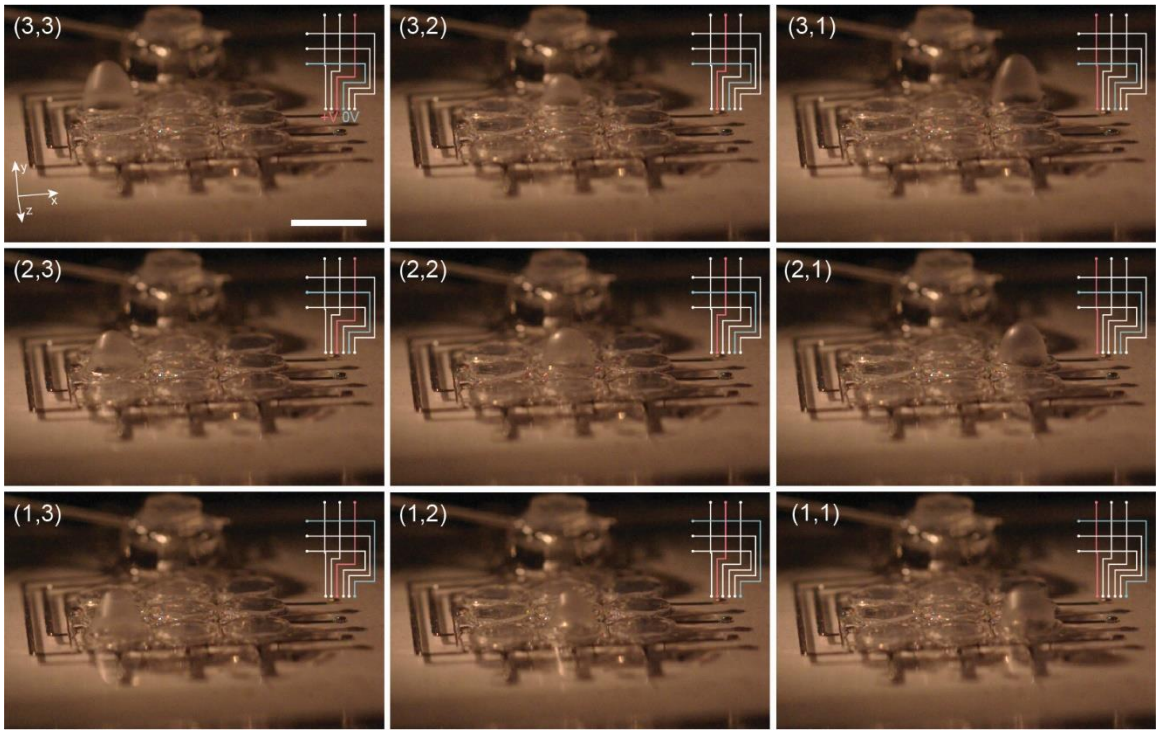

Fig. S9. Individual Performance of Arrayed Actuators. Panels display successful operation of each of the nine actuators. Array coordinates correspond to the (row, column) location of each actuation event, matching the electric trace operating diagrams at each panel's upper right corner. Downwards diagonal panels are given in Fig. 3c in the main text. Scale bar: 5 mm.

The tactile display demonstration incorporated a separate latching array of 3D-printed plastic pillars aligned directly above the actuators. These pillars had small magnets (SuperMagnetMan.com) at the bottom of each post. When brought close enough to magnets glued under the plate, the pillars remained in the upright position. Fig. S10 shows details of the latching

array's assembly and function. Relay switching times remained above 100 ms to minimize their impact on the microcontroller.

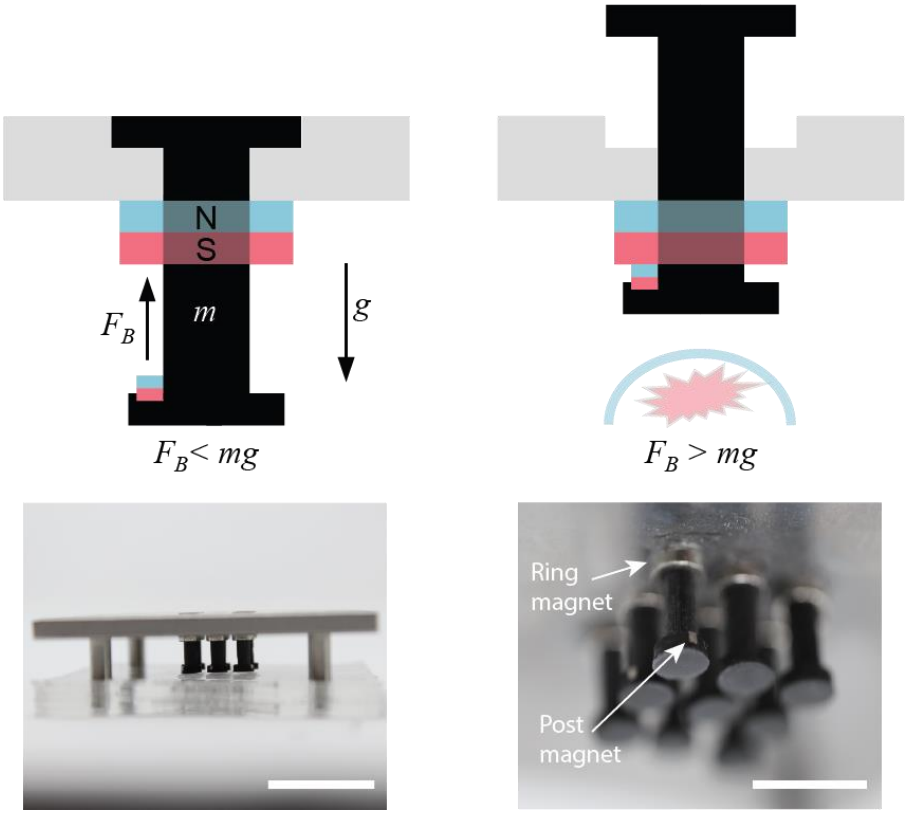

Fig. S10. Array Demonstration Latching Mechanism. Top two images show a diagram of the permanent magnet mechanism used in our braille demonstration. Bottom images show details of the latch assembly and its alignment with the arrayed actuator. Left image scale bar: 15 mm. Right image scale bar: 10 mm.

Fig. S11 shows additional images which spell out "orl" in braille (referring to the Organic Robotics Laboratory). If one wanted to spell "ORL", the bottom and most left-hand pillar would be raised alongside the other pillars; the "6" position of the preceding braille cell is raised to capitalize the following letter.

Fig. S11. Braille Tactile Display States. Programmed actuation sequences produce braille text. Image brightness and contrast increased to improve visibility. Scale bar: 5 mm.

3. Data Analysis Methods

3.1 Details on Actuator Performance Comparison. The disciplinary breadth and depth of research previously devoted to developing high density actuation arrays warrants a clear, equitable means of quantitatively comparing the technologies. For example: some actuators are pulsed, some can sustain their own deformation, and some are designed for vibrotactile purposes. Actuator A might operate at a higher frequency than actuator B, yet A might have a maximum displacement

orders of magnitude lower than B. Most of the literature do provide meaningful, qualitative comparisons that highlight general system advantages and disadvantages.

Given the small form factor of these devices, measurements of mechanical performance are also more difficult and may require expensive instrumentation. Fig. 1e, reproduced below as Fig. S12 (with accompanying citations), uses the three most reported actuator metrics (displacement, force, and response time) to provide a coarse quantitative comparison of the different power densities. Force and displacement are multiplied together to produce the stroke energy output plotted here. The approximate actuator volume coloration suggests that larger devices generally have the potential to produce greater energy outputs. We chose literature which reported sufficient performance metrics and featured an actuator intended for some haptic or tactile display application. We separately included one report (Table S1, Ref. 58) to capture the best performance of Hyperbraille-type systems (6).

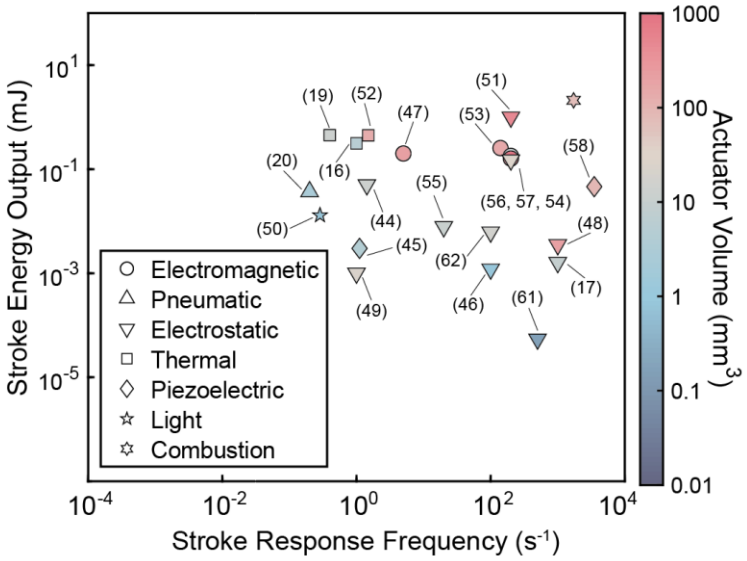

Fig. S12. Mechanical Performance Comparison with Citations. The triplicate citation reads left-to-right, plot points arranged from back to front.

Characteristic actuator surface area, thickness, force output, displacement output, and response time (the time to complete one upward stroke) were obtained from the literature. We believe that our figure roughly estimates metrics that optimal applications of the reported technologies can reasonably achieve. We have also reported these metrics with respect to their own experimental circumstances in Table S1, which shows the values of the plotted quantities with contextual annotations. For example, one annotation identifies which quantities are "experimentally correlated"; which quantities are co-obtained from a single measurement.

Main Text Ref. #	Actuation Strategy	Effective Surface Area (mm^2)	Thickness (mm)	Force Output (mN)	Stroke Output (mm)	Response Time (s)	Input Power (W)	Stroke Efficiency (%)
44	Electrostatic	0.69	20	50	**1**	**0.7**		
17	Electrostatic	4	2.3	**8**†	**0.2**	$7.9 \cdot 10^{-4}$‡	0.1	2.02
50	Light	1.80	0.4	**26**	0.5	**3.5***	.03	0.01
45	Piezoelectric	4	1	15	**0.2**	**0.9**		
46	Electrostatic	3.13	0.255	6	**0.2**	**0.01**		
47	Electromagnetic	36*	6	200	**1**	**0.2**		
16	Thermal	1.77	3	500	**0.7**	**1**	1.18	0.03
19	Thermal	7.02	2	**1500**†	**0.3**	**2.5**	0.1*	0.18
49	Electrostatic	100	0.25	**1**	1	**1**		
48	Electrostatic	228	1	**22**	0.16	**0.001**‡	0.07	5.33
20	Pneumatic	1.77	1.5[1]	66	**0.56**	**5**		
51	Electrostatic	50.4	10	1000	1	0.005‡		
52	Thermal	3.13	45	**320**†	**1.4**	**0.67**	6.8	0.01
53	Electromagnetic	12.3	13.08	160	1.59	0.007	1.4	2.54
54	Electromagnetic	1.77	5.5	300†	**0.6**	**0.005**	1	3.6
55	Electrostatic	1.77	6	13	**0.6**	**0.05**	0.003	5.2
56	Electrostatic	36	0.8	300	**0.5**	**0.005**	0.3*	10
57	Electromagnetic	64*	15*	200	**0.8**	**0.005**		
58	Piezoelectric	100	1	123	**0.38**	**$2.9 \cdot 10^{-4}$**‡		
59	Electrostatic	9	0.018	9†	**0.006**	**0.002**	0.003	0.9
60	Electrostatic	7.02	2.5	44	**0.14**	**0.01**		
N/A	Combustion	25	3.5	**1.7**† mJ		**$5.8 \cdot 10^{-4}$**		See §3.2

Table S1. Actuator Performance Comparison Metrics. Dataset (Main Text, Refs. 16, 17, 19, 20, 44-60) used to generate a graphical performance comparison (Figs. 1e, S12) is numerically reproduced here. This paper formally reports the actuator membrane work output; force and displacement cells are combined to reflect this. Quantities in **bold** are taken from the same measurement and are thus "experimentally correlated". Quantities that were pictorially, graphically, or quantitatively inferred are denoted with (*). Non-blocked force measurements are denoted with (†). Response times which are the reported maximum or resonant frequencies are denoted with (‡). Input power and operational efficiency are shaded in gray because they are not considered in Figs. 1e, S10. Stroke efficiency is calculated from given quantities. Input power metrics could be found for literature with empty rows.

Though we do not compare input power and efficiency from the literature with our device, we provide available values in Table S1 for reference. Because the power associated with an instance of electric breakdown is difficult to measure or approximate, we only report common ignition energy values in this paper.

3.2 Actuator Stroke Efficiency. Because we allow reactant gas to passively flow through our prototype actuator, we must accept that a significant portion of stored gas is exhausted, making the true system efficiency low. Future systems could recirculate gas or control flow from the initial fuel channel junction (plenum). While a combustion engine's cycle efficiency is comparable to that of a thermodynamically ideal heat engine, we consider here the "stroke efficiency" η_s to understand how well the chemical energy present in the cylinder converts to the mechanical work done by the heated gas on the membrane and external boundary:

$$\eta_s = \frac{|W_s|}{\left|\Delta h_{HHV} m_{CH4} + U_{ig}\right|},$$

where Δh_{HHV} is the higher heating value (HHV) combustion enthalpy, m_{CH4} represents the mass of fuel in the cylinder, and U_{ig} is the electrical ignition energy. The HHV includes the energy released from product water condensation (see Movie S4 caption), which the lower heating value (LHV) does not (3). For methane, Δh_{HHV} = 55 kJ g^{-1}. Therefore, ~200 mJ of chemical energy is present in the cylinder. Values for U_{ig} are typically 10-30 mJ (7). Then, η_s = 0.71%. A purely hydraulic power transmission strategy may fully capture the total stroke work (W_s) done by the membrane, yet flexural or linkage-based transmission will reduce the effective stroke work due to membrane conformation (SI Appendix, 2.3).

Another way one can calculate the efficiency is by simply ignoring the stored chemical energy, since it is simply a property of the gas which requires no active pumping or forcing to move (the flow is pressure driven). Then, only electrical energy would be considered in the denominator of a separate "operational efficiency" calculation:

$$\eta_s = \frac{|W_s|}{|U_{ig}|}.$$

Taken this way, the efficiency then becomes η_s = 5.5%, closer to some metrics in Table S1.

3.3 Experimental Image Processing. Side-profile high speed video data (Fig. 1b) provided the basis to estimate membrane volume, stretch, and displacement quantities. We developed a custom MATLAB script which extracts membrane edge data in a two-step fashion. First, it removes all but essential membrane edge data, and second, it refines the pixel data until only one pixel per y position per half remains. We used the MATLAB Image Processing Toolbox™ and the "bwconncomp" function to distinguish actual membrane edge pixel data from the rest of the video. Fig. S13 shows one frame and the two rounds of data filtration to produce data which was analyzed. Axisymmetric assumptions of the deformed membrane shape allow us to infer the principal stretches and inflated volume.

Fig. S13. Image Analysis for Membrane Characterization. A MATLAB script imports video data and iteratively refines essential membrane data for membrane deformation characterization. Scale bar: 3 mm.

3.4 State Variable Estimation from Video. With membrane edge profiles, we empirically obtained our performance metrics by calculating three quantities in each video frame: displacement, volume, and membrane stretch. Displacement was calculated by picking the highest pixel from each frame. Observations from high-speed videos show slightly asymmetric membrane dynamics since it has many small oscillations within its general inflation and deflation. Therefore, we estimated the frame volume by splitting each frame in half and averaging the two calculated volumes. For frame i, the volume V_i for each membrane half is given by a simple Riemann sum approximation of the disc

integration method:

$$V_i = \pi \int_0^{\delta} r^2(y)dy \approx \sum_{j=1}^{n} \pi r_j^2 h_p$$

Pixel height is given by h_p. The upper integration bound at point (0, δ) is the highest and centermost point of each membrane half. Membrane stretches were calculated by organizing the set of pixels from left to right, calculating the distance of each pixel from leftmost to rightmost using the distance formula, then summing those distances.

3.5 Experimental Frequency Response Analysis. The function generator's high precision voltage output consistently generated sparks on time. Actuator displacement for each period was calculated by finding the maximum of the set of points generated by the MATLAB "peaks" function. Each set of time-series data was obtained at one frequencies; the data plotted in Fig. 1f of the main text are an average of the set of maxima.

For the intermediate sparking range (vertical dotted lines in Main Text, Fig. 1f), data analysis showed a substantial increase in the displacement variance. Figure S14 gives a more detailed picture of the frequency response profiles, showing that the low-frequency spike in variance is a stable, repeating sawtooth pattern (35 Hz).

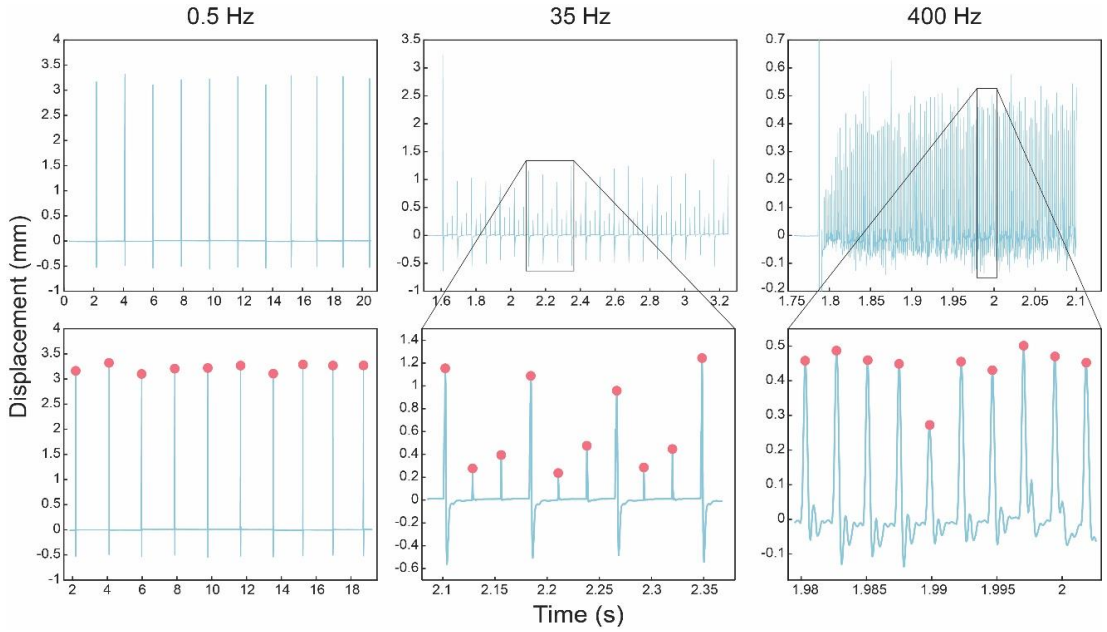

Fig. S14. Frequency Response Displacement Variance Over Scales of f_{sp}. Peak displacement for three different spark frequencies f_{sp}: 0.5 Hz, 35 Hz, and 400 Hz. Displacements under 0 mm occur because the membrane is underdamped and deflects into the cylinder, possibly by negative pressure fluctuations. Constant flowrate Q = 1.2 mL s^{-1} for all plots. Bottom panels are ten-peak samples taken from the upper panels. Graph shows consistent actuation at 0.5 Hz and noisy actuation (σ = 0.6μ, including initial ramp to steady state) at 400 Hz. At 35 Hz, a clear, stable ramping (sawtooth) pattern is evident in the bottom panel. Review of the top 35 Hz panel seems to also reveal a lower frequency oscillation of the highest peaks.

In Section 4.3, we describe a model developed to address these unexpected results. To conclude this section, we note that the acoustic wave produced by electric breakdown is significant enough to cause perceivable membrane transduction (by a finger placed on the membrane). Given the measurement noise and relatively small displacements at high frequencies, we checked that acoustic contributions did not come to dominate membrane actuation. We found that the spark

produced ~15 μm displacements in the single actuator device. While likely not a useful mechanism for this report's applications, spark-based acoustic microactuation could be explored in a manner like work by Ji et al. (see Table S1, Ref. 59 for metrics).

4. Theory

4.1 Neo-Hookean Membrane Assumption for Elastic Energy Estimation. In this work, the 0.5 mm thick, 5 mm diameter hyperelastic membrane serves as a deformable piston, a moving system boundary by which the combusted gas can do work. In the process, the membrane stretches, storing additional elastic energy. This energy storage mode helps the membrane snap back quickly and repeatably, but reduces the energy which can go to doing external work. Therefore, we compared the work of stretching the membrane with pV work done by the inflated membrane on the atmosphere.

Section 4.1 of Long, Shull, and Hui gives a thorough derivation and discussion of modeling the quasistatic free inflation of a hyperelastic membrane (8). As our experiments featured highly complex, transient, aspherical membrane dynamics (equilibrium assumption requires a nearly spherical membrane shape), we obtained a strain energy estimate by calculating the strain energy of an equivalent flat membrane pulled equibiaxially outward. This assumption is supported by the membrane's virtually negligible flexural rigidity ($D \approx \frac{1}{3}\mu h^3 \ll 1$, μ is shear modulus), which we experimentally verified by observing the sharp bending angles at the membrane base (Movies S1—S3). We chose to represent the membrane as an incompressible (J = 1) neo-Hookean solid after reviewing data supplied for Ecoflex 00-30 (9). Then, the strain energy density function is given by

$$\psi = \frac{\mu}{2}(I_1 - 3);\ I_1 = tr(\mathbf{F}^T\mathbf{F}),$$

where **F** is the deformation gradient. From the biaxial stretch assumption (Cartesian coordinates),

$$\lambda_1 = \lambda_2 \equiv \lambda_p,$$

$$J = 1 = \lambda_1\lambda_2\lambda_3 \Rightarrow \lambda_3 = \frac{1}{\lambda_p^2},$$

allowing us to specify **F** and express ψ in terms of λ_p:

$$\mathbf{F} = \begin{bmatrix} \lambda_p & 0 & 0 \\ 0 & \lambda_p & 0 \\ 0 & 0 & 1/\lambda_p^2 \end{bmatrix},$$

$$\psi = \frac{\mu}{2}\left(2\lambda_p^2 + \frac{1}{\lambda_p^4} - 3\right).$$

Reducing the expression to a single independent variable conveniently allows for an estimate using 2D membrane data. For the highest reported stretch ratio, the strain energy Ψ (here, $\Psi = \psi V_0$ since we assume J = 1) is 1.7 mJ.

4.2 Laminar Flame Propagation Model (LFP). We were interested to understand the flame's behavior more precisely in our actuator, having design, material, and geometric qualities uncharacteristic of typical combustion-powered machinery. We began by comparing the video measurements to a 1D multi-zone model (Cantera v2.4.0, Python 3.8). The model comprised an adiabatic combustion cylinder having the same initial dimensions as our single cylinder design. A

massless piston represented a membrane with no stiffness and provided an upper limit on the gas' actuation potential. Some simulations featured an added spring to capture membrane elasticity.

At each time-step, our model first computes the energy released from the incremental flame expansion. We assume an infinitesimally thin flame so that there can be two, discrete composition zones: the burnt products behind the flame front, and the unburnt, premixed reactants in front of the flame front. The model then numerically solves for the updated specific volume using the first law of thermodynamics. For some simulations, a spring term added a variable force to capture an idealized, linear membrane elasticity.

With a known, incremental heat injection, the new gas equilibrium state variables may be determined. In this derivation, we denote mixture volume, temperature, pressure, and internal energy at a given timestep n as V_n, T_n, p_n, and U_n, respectively. We model the flame propagation and adiabatic heat addition by assuming that a small ignition kernel (an approximate spark), grows outwardly as a sphere, or

$$\frac{dV_{fl}}{dt} = 4\pi r_{fl}^2(t)s_L,$$

where $s_L = dr_{fl}/dt$ is the unconfined laminar flame speed. Since s_L is highly dependent on the present mixture species (and concentrations), we calculate $s_L(\Phi)$ using a 1D flame object and the GRI 3.0 mechanism (10). Then, we calculate the total heat release at timestep n by multiplying the incremental volumetric flame expansion by the incremental heat release (11):

$$q_{fl} = \frac{Q_{fl}}{V_{fl}} = \Delta t\dot{\omega}_T = -\Delta t\sum_{k=1}^{N}\Delta h_{f,k}^{o}\dot{\omega}_k,$$

where the heat release rate q_{fl} is calculated by summing over the enthalpy release rates of all present species. By obtaining the heat release from the more detailed combustion theory, we use a simpler ideal gas analysis to develop the rest of the model.

Beginning with the first law of thermodynamics,

$$dU = \delta Q - \delta W,$$

we express the change in internal energy as a function of the external pressure-volume boundary work W_b done by the gas (adiabatic cylinder assumption implies that $\delta Q = Q_{fl}$),

$$U_{n+1} - U_n = m(u_{n+1} - u_n) = mc_v(T_{n+1} - T_n) = Q_{fl} - m\int_n^{n+1} p(v)dv.$$

Lowercase letters are used to specific (mass-independent) forms of extensive quantities (except p). At each time step, the gas must be in equilibrium; we may write p_{n+1} explicitly as

$$p_{n+1} = p_{atm} + \frac{K\delta}{A_{cyl}},$$

Where A_{cyl} is the piston area, δ is the total spring displacement in the interval $[t_n, t_{n+1}]$, and K is the spring constant. When $K = 0$, the entire process is also isobaric and represents behavior of a truly unconfined, ideal gas under atmospheric pressure. To integrate the above equation, we express δ in terms of v:

$$\delta(v) = \frac{vm}{A_{cyl}} - h_{cyl}.$$

Then, w_b becomes

$$w_b = \int_{v_n}^{v_{n+1}} p_{n+1}(v')dv' = \left(p_{atm} - \frac{K}{A_{cyl}}h_{cyl}\right)(v_{n+1} - v_n) + \frac{Km}{2A_{cyl}^2}(v_{n+1}^2 - v_n^2).$$

Next, we considered the flow energy of the intake and exhaust gases, given as

$$E_{in} = \dot{m}_{in}\left(h_{in} + \frac{1}{2}c_{in}^2\right)$$

and

$$E_{out} = \dot{m}_{out}\left(h_{out} + \frac{1}{2}c_{out}^2\right).$$

These terms account for the change in internal energy from mass transfer. We use *c* as velocity to avoid confusing velocity and specific volume. They do not vary with cylinder pressure. While we incorporated the flow energy terms in this simulation, their omission changed the final volume result by ~1%. Thus, we omit them from the remainder of this derivation. We treat the mass exchange terms more sensitively in Section 4.3, where intake and exhaust are pressure-driven, species-dependent flows.

Lastly, T_n can be calculated from the known pressure and volume with the ideal gas law, too becoming a function of *v*:

$$T_{n+1} = \frac{p_{n+1}v_{n+1}}{R} = \frac{v_{n+1}}{R}\left(p_{atm} + \frac{Km}{A_{cyl}^2}v_{n+1} - \frac{Kh_{cyl}}{A_{cyl}}\right).$$

The first law can now be written completely in terms of *v* and known quantities,

$$Q_{fl} = \frac{mc_v v_{n+1}}{R}\left(p_{atm} + \frac{Km}{A_{cyl}^2}v_{n+1} - \frac{Kh}{A_{cyl}}\right) - mc_v T_n + m\left(p_{atm} - \frac{K}{A_{cyl}}h_{cyl}\right)(v_{n+1} - v_n) + \frac{Km^2}{2A_{cyl}^2}(v_{n+1}^2 - v_n^2),$$

where we numerically solve for v_{n+1} and obtain the next set of state variables.

The LFP focuses on the behavior of the flame, revealing the approximate actuation timescale for an adiabatic flame in a linear piston with the same initial dimensions as the single cylinder actuator. By decoupling the intake and exhaust ports from pressure-dependent flows, we consider the maximum pV work an ideal gas can contribute. Comparing this model to experimental data shows discrepancies in displacement and actuation speed. The difference in displacement is expected due to the heat transfer and exhaust flow assumptions, yet the slower laminar flame speed indicates to us that there are additional mechanisms driving the flame propagation. While this difference may seem like a mere artifact of our device design, we believe that a deeper scientific understanding of the small-scale flame interactions will prove to be a useful design tool for future soft microcombustion technology.

4.3 Linearized Fluid-Structure Interaction Model (LFSI). The unexpected displacement patterns observed at intermediate sparking frequencies (10 Hz-100 Hz) led us to develop a linearized fluid-structure interaction model (LFSI) that couples an ideal gas with a linear elastic membrane and an open exhaust port (the intake flow is set as a constant). We assume the ideal gas to be a well-mixed composition of the major species, with all chemistries occurring instantaneously. Therefore, the LFSI assumes that combustion is a nearly instantaneous heat addition. The well-mixed assumption allows us to use an integral approach in the numerical solution.

While we first attempted to treat the membrane as a neo-Hookean material, we found the quasistatic membrane assumption required for the model incompatible with the data from our frequency response experiments. The fast membrane dynamics produce oscillating and aspherical membrane shapes (Movies S1-S3), an additional discrepancy between data and an assumed spherical center displacement. For simplicity, then, we use a linear model appropriate for small deformations (12), expressing the plate displacement w_m as

$$w_m(r) = \frac{3(1-\nu^2)}{80Eh^3}\left(r_{cyl}^2 - r^2\right)^2 (p(t) - p_{atm}),$$

where E is the elastic modulus, ν is Poisson's ratio, h is the membrane thickness, r_{cyl} is the membrane radius, and p is the cylinder pressure. By integrating the above equation, we can relate the cylinder pressure and total volume:

$$V(t) = V_{cyl} + 2\pi \int_0^{r_{cyl}} w(r) r dr = V_{cyl} + \frac{\pi r_{cyl}^6 (1-\nu^2)}{80Eh^3}(p(t) - p_{atm}).$$

We treat the major reactants and products of the global methane-oxygen reaction (see Main Text, Equation 1) as separate ideal gases. Methane and oxygen are injected into the chamber at a constant rate. At a prescribed frequency, the instantaneous combustion step adds heat energy proportional to the methane present in the cylinder. We also consider the possibility that negative pressure differentials cause ambient air to be sucked back into the cylinder through the exhaust port. Here, ambient air is a room temperature gas mixture of 79% nitrogen and 21% oxygen. We assume that, although the kinetics will be slower with nitrogen present, they can still be approximated as instantaneous.

The ideal gas law is written as

$$p(t) = \rho(t) R_{sp}(t) T(t),$$

where ρ is the density and R_{sp} is the mass-specific gas constant. R_{sp} is iteratively calculated using the updated species masses (including nitrogen):

$$R_{sp}(t) \equiv R \sum_{species} \frac{\frac{m_i(t)}{M_i}}{\sum_{species} m_i}.$$

R is the universal gas constant and M_i is the species molar mass. Density is also iteratively calculated;

$$\rho(t) = \frac{1}{v(t)} = \frac{1}{V(t)} \sum_{species} m_i.$$

Here, v is the specific volume.

In the LFSI, we treat the exhaust mass flow rate $\dot{m}_{out}$ as a pressure-dependent Hagen-Poiseuille flow through a circular cross-section,

$$\dot{m}_{out}(t) = \frac{\pi r_e^4 (p(t) - p_{atm})\rho(t)}{8 l_e \mu},$$

with r_e and l_e respectively representing the exhaust port radius and total length (losses from the 90° elbow are neglected). The proportionality constant μ is the dynamic viscosity of the gas. This equation assumes nearly incompressible flow; the low pressures we calculate justify this assumption. Then, we can write the system mass conservation equation as

$$\dot{m}_{in} - \dot{m}_{out}(t) = \frac{d}{dt}\big(\rho(t)V(t)\big).$$

Mass conservation of the individual species requires additional discontinuous functions for $\dot{m}_{out}$ to account for the discrepancy in ambient and internal gas compositions. We define these as

$$\dot{m}_{out}^{+}(t) = \begin{cases} \dot{m}_{out}, & \dot{m}_{out} > 0 \\ 0, & \dot{m}_{out} \leq 0 \end{cases}$$

$$\dot{m}_{out}^{-}(t) = \begin{cases} 0, & \dot{m}_{out} \geq 0 \\ \dot{m}_{out}, & \dot{m}_{out} < 0 \end{cases}.$$

Then, the species mass conservation equations become

$$\frac{dm_{CH_4}}{dt} = Y_{in}^{CH_4}(\Phi_{in})\dot{m}_{in}(t) - \left(\frac{\dot{m}_{out}^{+}(t)}{\rho(t)V(t)}\right) m_{CH_4}(t) - M_{CH_4}\alpha(t)$$

$$\frac{dm_{O_2}}{dt} = \left(1 - Y_{in}^{CH_4}(\Phi_{in})\right)\dot{m}_{in}(t) - \left(\frac{\dot{m}_{out}^{+}(t)}{\rho(t)V(t)}\right) m_{O_2}(t) - 2M_{O_2}\alpha(t) - 0.21\dot{m}_{out}^{-}(t)$$

$$\frac{dm_{CO_2}}{dt} = M_{CO_2}\alpha(t) - \left(\frac{\dot{m}_{out}^{+}(t)}{\rho(t)V(t)}\right) m_{CO_2}(t)$$

$$\frac{dm_{H_2O}}{dt} = 2M_{H_2O}\alpha(t) - \left(\frac{\dot{m}_{out}^{+}(t)}{\rho(t)V(t)}\right) m_{H_2O}(t)$$

$$\frac{dm_{N_2}}{dt} = -\left(\frac{\dot{m}_{out}^{+}(t)}{\rho(t)V(t)}\right) m_{N_2}(t) - 0.79\dot{m}_{out}^{-}(t),$$

where $Y_{in}^{CH_4}$ is the input methane mass fraction (intake gas comprises just methane and oxygen), written as a function of the input equivalence ratio Φ_{in}:

$$Y_{in}^{CH_4}(\Phi_{in}) = \frac{\left(\frac{f}{o}\right)_{st}\Phi_{in}}{\left(\frac{f}{o}\right)_{st}\Phi_{in} + 1},$$

$$\left(\frac{f}{o}\right)_{st} = \left(\frac{m_{fuel}}{m_{oxidizer}}\right)_{stoich} \approx 0.25.$$

$Y_{in}^{CH_4}$ does not represent the mass fraction of methane in the cylinder, only the intake setpoint. The reaction function α was introduced into the conservation equations to smooth the computation. We implemented α in the code as a sum of probability distribution functions (PDFs) placed at the sparking frequency we prescribe:

$$\alpha(t) = \sum_{k=1}^{n} e^{\left(-\frac{\left(t-\frac{k}{f_{sp}}\right)^2}{2\sigma^2}\right)}.$$

Each Gaussian pulse has a standard deviation σ of 1 μs, a negligible time scale when compared to membrane dynamics. The sparking frequency is specified by f_{sp}. The units of α are in s^{-1} (for consistency, since the area under α is equal to 1); in the species conservation equations, the molar mass M_i multiplied by the forward reaction stoichiometric coefficient (methane equation term is multiplied by -1) provides the magnitude of the total species consumption rate term. The total number of pulses is specified by n. When no methane remains, α immediately becomes zero.

Finally, the energy conservation equation is given here as

$$\frac{d}{dt}\left(c_p V(t) T(t)\right) = -h_t \pi r_{cyl}^2 (T(t) - T_{atm}) + \Delta H_{CH_4} \alpha(t) + c_p T(t)\left(\dot{m}_{in} - \dot{m}_{out}(t)\right) - p(t)\frac{dV(t)}{dt},$$

where the LHS is the change in internal energy in the chamber. In the RHS, the first term represents convective heat transfer, the second term represents heat generated by methane consumption, the third term represents the heat of advection, and the fourth term represents the pV work done by the gas at the elastic system boundary.

All parameters were estimated with characteristic values and the resulting equations were solved numerically using Mathematica. The estimations of the different coefficients and the numerical solutions are presented in the SI code.

Fig. S15 shows displacement data and species dynamics from simulated 35 Hz operation. In Fig. S15a, we can see initial qualitative agreement with experimental observations, such as the large initial displacement followed by a steady state, lower magnitude actuation cycle. Further, we see that the membrane overshoots after deflation, with an accompanying rise in ambient oxygen and nitrogen (Fig. S15b).

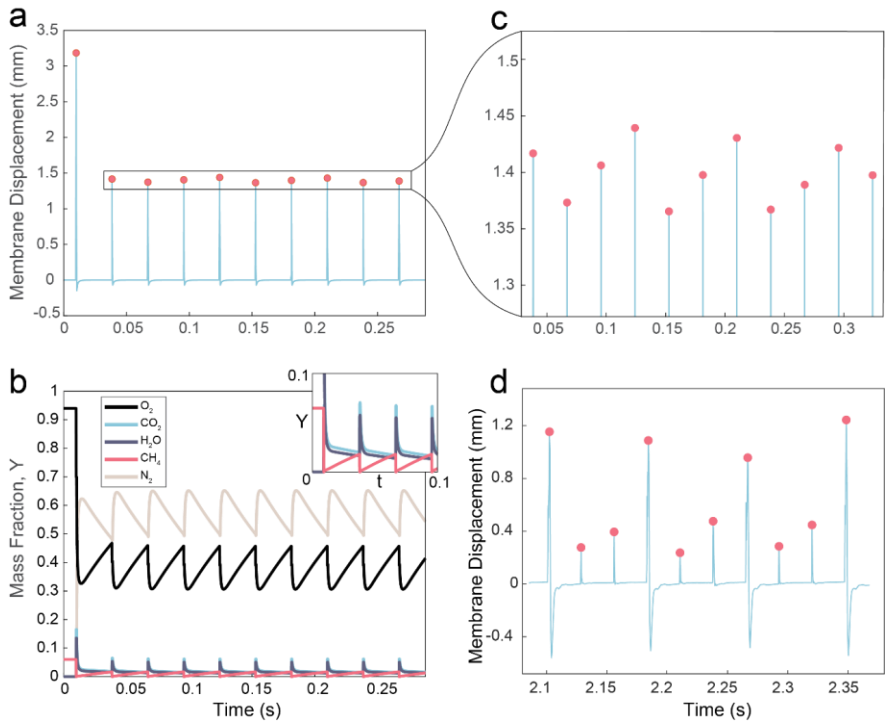

Fig. S15. Comparing LFSI with Experimental Data. Axis scales vary by panel. (a) LFSI-generated cyclic displacement data for 35 Hz actuation. Each peak accompanied by slight membrane overshoot. First combustion significantly higher than others because chamber is purely reactant gas at the start. A zoomed view is provided in (c) to compare to experiment. (b) Theoretical species dynamics. At a given spark frequency, gases reach a dynamically stable configuration. Inset shows low-Y gases (O_2, H_2O, CH_4) more clearly. (c) A significantly reduced sawtooth pattern is present in the LFSI with a total height difference of about 100 μm. (d) Experimental data from Fig. S14 is reproduced for comparison.

This remains a qualitative result as we have done no experimental gas analysis to verify these predictions. However, we believe that the simulated presence of the overshoot and sudden increase in ambient gases support our hypothesis that a suction (negative pressure) mechanism can affect the subsequent combustions.

Though we can capture much of the actual device behavior using the LFSI, we have not yet successfully reproduced the experimental sawtooth pattern we seek to explain. Close examination of the 35 Hz LFSI displacement plot (Fig. S15c) does in fact reveal a small (range of 100 μm) ramping pattern in the displacement peaks relative to what we see in experiment (Fig. S15d). The other largest discrepancy between model and experiment is the magnitude of membrane overshoot. Given that we believe the overshoot is causally related to the next combustion, it seems reasonable to conjecture that a larger overshoot would bring in more ambient air to deaden the next combustion. Yet, the material properties and geometries we chose seem to otherwise match the model.

A more sensitive treatment of the fluid-structure behavior is likely needed to account for this phenomenon. Nonlinear membrane elasticity may influence the membrane displacement at highly stretched configurations. We are also interested in the importance of the intake channel; in reality, it is a pressure-driven flow through an open tube, subject to cylinder pressure fluctuations.

Legends for Supplementary Movies

Movie S1. Single actuation at $\Phi = 0.20$.

Movie S2. Single actuation at $\Phi = 0.27$.

Movie S3. Single actuation at $\Phi = 0.34$.

Movie S4. 50 Hz actuation cycles at $\Phi = 0.27$. Talcum powder (see SI Appendix, 2.3) did not coat this actuator's surface. Cylinder walls, channels, and port locations can be seen at bottom. A less consistent ramping pattern similar to the 35 Hz case occurs. Cylinder wall water condensation can be seen fluctuating throughout the movie. Membrane bows slightly outwards due to higher flow rate: Q = 2 mL s^{-1}.

Movie S5. Manual array actuations at $\Phi = 0.32$. Individual actuations were selected by manually controlling relays. Selection corresponds to Fig. 3c in main text. Fig. S9 contains stills of the other actuators in operation.

Movie S6. Tactile Display Demonstration: "CH4". Computer-controlled protocols produced persistent array display states.

SI References

1. N. Runyan, D. Blazie, EAP actuators aid the quest for the "Holy Braille" of tactile displays in *Electroactive Polymer Actuators and Devices (EAPAD) 2010*, (SPIE, 2010), p. 764207.
2. P. Horowitz, W. Hill, *The Art of Electronics*, 3rd Ed. (Cambridge University Press, 2015).
3. Stephen R. Turns, *An Introduction to Combustion: Concepts and Applications*, 3rd Ed. (McGraw-Hill Education, 2011).
4. E. Verron, R. E. Khayat, A. Derdouri, B. Peseux, Dynamic inflation of hyperelastic spherical membranes. *Journal of Rheology* **43**, 1083–1097 (1999).
5. R. F. Shepherd, *et al.*, Using explosions to power a soft robot. *Angewandte Chemie - International Edition* **52**, 2892–2896 (2013).
6. R. J. Wood, E. Steltz, R. S. Fearing, Optimal energy density piezoelectric bending actuators. *Sensors and Actuators, A: Physical* **119**, 476–488 (2005).
7. John B Heywood, *Internal Combustion Engine Fundamentals*, 1st Ed. (McGraw-Hill Education, 1988).
8. R. Long, K. R. Shull, C. Y. Hui, Large deformation adhesive contact mechanics of circular membranes with a flat rigid substrate. *Journal of the Mechanics and Physics of Solids* **58**, 1225–1242 (2010).
9. C. Larson, *et al.*, "Highly stretchable electroluminescent skin for optical signaling and tactile sensing."
10. G. P. Smith, *et al.*, GRI 3.0 Mechanism. *combustion.berkeley.edu/gri-mech/version30/text30.html*.
11. T. Poinsot, D. Veynante, *Theoretical and Numerical Combustion*, 2nd Ed. (R.T. Edwards, Inc., 2005).
12. S. P. Timoshenko, S. Woinowsky-Krieger, *Theory of Plates and Shells* (McGraw-Hill, 1959).